



Experimental study on seismic behaviour of an innovative composite shear wall

Shao-Teng Huang^a, Yan-Sheng Huang^{a,b}, An He^{a,c,*}, Xu-Lin Tang^{a,d}, Qing-Jun Chen^{a,b}, Xinpei Liu^e, Jian Cai^{a,b}

^a School of Civil Engineering and Transportation, South China University of Technology, Guangzhou 510640, PR China

^b State Key Laboratory of Subtropical Building Science, South China University of Technology, Guangzhou 510640, PR China

^c School of Civil and Environmental Engineering, Nanyang Technological University, 50 Nanyang Avenue, 639798 Singapore, Singapore

^d Guangzhou Jishi Construction Group Co., Ltd., Guangzhou 510115, PR China

^e Centre for Infrastructure Engineering and Safety, The University of New South Wales, UNSW, Sydney 2052, Australia

ARTICLE INFO

Article history:

Received 19 December 2017

Received in revised form 15 April 2018

Accepted 2 May 2018

Available online xxxx

Keywords:

Concrete filled steel tube (CFST)

Composite shear wall

Experimental study

Cyclic test

Seismic behaviour

Transverse stiffeners

ABSTRACT

To improve the strength and ductility of the core walls in high-rise buildings which would be subjected to combined high axial compressive force and bending moment during the earthquake, an innovative concrete filled double-skin steel-plate composite (CFDSC) wall is proposed. The CFDSC wall is composed of the concrete filled double-skin steel-plate wall body with transverse stiffeners, vertical diaphragms and distributed batten plates welding on the internal surface of the double steel plates, and the concrete filled steel tube (CFST) columns including a pair of CFST columns positioned at the end of the cross section as boundary elements and an additional one located in the central section of the wall. Five CFDSC wall specimens were tested under constant axial compressive force and lateral reversed cyclic loading to investigate the seismic behaviour of the wall considering the effect of axial force ratio and shear span ratio. The favourable seismic performance of the CFDSC walls was demonstrated in the test. No serious pinching effect was observed on the hysteresis curves of all the specimens. The drift ratios corresponding to the ultimate stage were recorded as being in the range from 1/67 to 1/30 and the ductility coefficients were varied from 4.50 to 8.22. The experimental results manifest that the CFDSC walls have great energy dissipation capacity. Formulae for calculating the lateral load-carrying capacity of the CFDSC wall, taking the confinement effects from steel plates into account, were proposed. The results calculated by the proposed method show good agreement with the experimental results.

© 2017 Elsevier Ltd. All rights reserved.

1. Introduction

The reinforced concrete (RC) shear walls are critical structural components to resist the lateral force in high-rise buildings. In recent years, constructions of high-rise buildings are increasing rapidly in China, while the conventional RC shear wall might not be able to provide sufficient resistance to the seismic loading combinations, particularly for the walls located at the lower stories which are usually subjected to substantial axial compressive force and bending moment. To satisfy the seismic design requirement of high-rise buildings in earthquake zone, the concrete filled double-skin steel-plate composite (CFDSC) wall, which consists of two steel faceplates on the exterior surfaces and the infill concrete, is becoming increasingly attractive as the main lateral resistance component. The CFDSC wall takes advantages of both RC wall and steel plate wall [1]. The infill concrete could prevent the concave local buckling of the steel plates, and thus improves

the anti-local buckling capacity of the steel faceplates, while the strength and ductility of the inner concrete are enhanced due to the confinement from the outer steel plates. By the reason of its excellent mechanics performance, the thickness of CFDSC wall could be much smaller than that of the conventional RC wall, which could reduce the weight of building and increase the usable floor area [2]. Furthermore, the construction process of the CFDSC shear wall is also quite efficient since the steel faceplates could act as permanent formwork. It has been proved that the CFDSC wall performed high lateral resistance and excellent energy-dissipating capacity, and thus has been adopted in several high-rise buildings to replace the traditional RC shear wall [3,4].

Various types of CFDSC wall and the corresponding design recommendations have been proposed and reported in the existing literatures. A CFDSC wall comprising of vertically aligned profiled steel sheeting and infill concrete was firstly conceived by Wright et al. [5], and its axial compressive, flexural and shear behaviour were further investigated [1,6–8]. To strengthen the combination between the steel plates and the infill concrete, tie bars, tie bolts, stiffeners or vertical diaphragm were adopted in the CFDSC system. Eom et al. [2] tested

* Corresponding author at: School of Civil Engineering and Transportation, South China University of Technology, Guangzhou 510640, PR China.

E-mail address: an.he@mail.scut.edu.cn (A. He).

three isolated and two coupled CFDSC walls connected by tie bars with rectangular and T-shaped cross sections under in-plane cyclic loading. The use of tie bars was also introduced by Ji et al. [9] and Chen et al. [10]. However, the construction of tie bars or tie bolts requires complex welding process. Moreover, Nie et al. [11–13] studied the cyclic behaviour of the CFDSC walls using high-strength concrete with vertical diaphragms. Zhang et al. [14] developed the bundled lipped channel-concrete T-shaped composite wall, which is comprised of a cold-formed square hollow section in the centre and two cold-formed lipped channels at each side to form the flange of the wall. Generally, the experimental results of the CFDSC wall with the aforementioned configurations exhibited great mechanical properties with high ductility and energy dissipation capacity. Compared with the ones with tie bar or tie bolts, the CFDSC walls with vertical diaphragms, stiffener or distributed batten plates showed better seismic performance [11,15,16].

Recently, an innovative CFDSC wall was presented and adopted in the China Southern Airlines Building in Guangzhou, China, as Fig. 1 shows. The total height of the China Southern Airlines Building was 150 m, and the thickness of the innovative CFDSC wall was only 220–500 mm. This innovative CFDSC wall was composed of the concrete filled double-steel-plate wall body and the CFST columns, as shown in Fig. 2. A pair of CFST columns was positioned at the end of the cross section to perform as boundary

elements, while an additional one was in the central section of the wall to segment the wall into appropriate parts. The CFST columns were connected by the double steel faceplates. In order to enhance the contact between the steel faceplates and the infill concrete and reduce the effective width of the steel faceplate for alleviating the local buckling effects, the transverse stiffeners and vertical diaphragms were welded on the internal surface of the steel plate and the steel plates were divided into several compartments. At the centre of each steel compartment, a batten plate was attached between the double steel plates for further strengthening the connection between the inner concrete and the steel plate. The proposed configuration is expected to not only augment the seismic performance of the CFDSC wall but also simplify the construction process, which consequently reduces the cost. The deformation capacity of the CFDSC wall could be enhanced significantly by the employment of CFST boundary elements [16,17] and the reinforcements which combine the double steel plates and the inner concrete into integration. The CFST column located in the middle of the section separates the whole steel plate into small part, which leads to more convenient welding of the inner reinforcements and easier achievement of modular production. The avoidance of serried tie bars or tie bolts welding in the steel plate could also simplify the construction procedure.



(a) Architectural rendering



(b) Photo of building site



(c) Installation of composite shear wall



(d) Hoisting of composite shear wall

Fig. 1. China Southern Airlines Building.

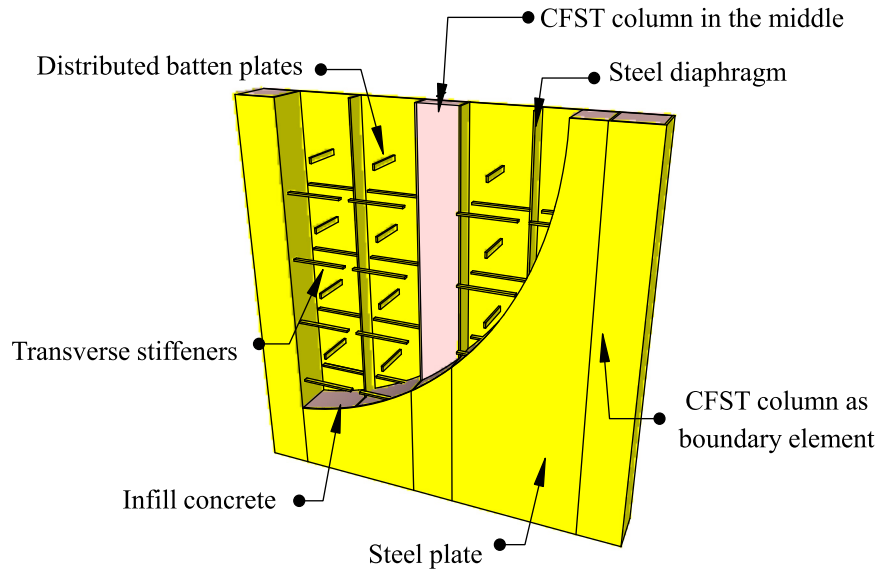


Fig. 2. Innovative composite shear wall in China Southern Airlines Building.

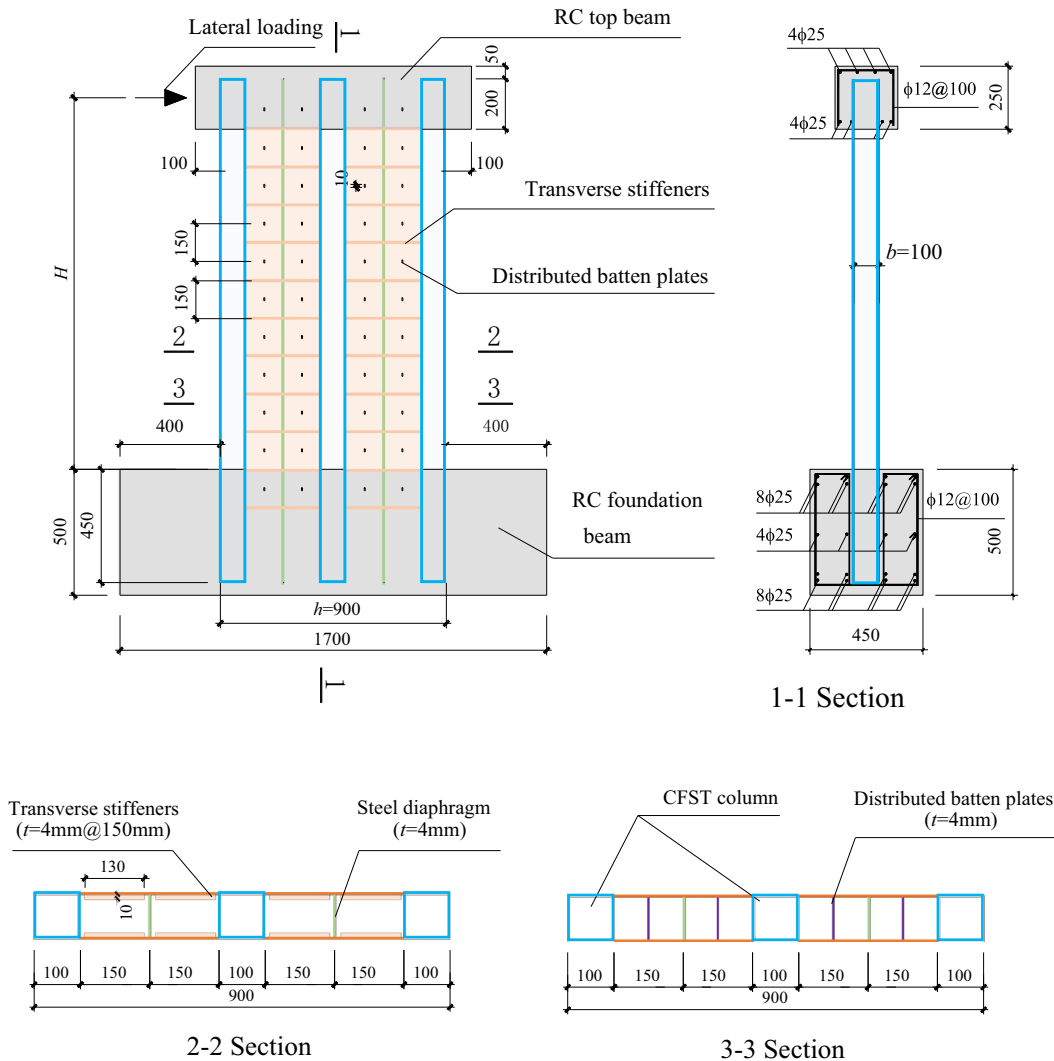


Fig. 3. The details of the specimens (Units:mm).

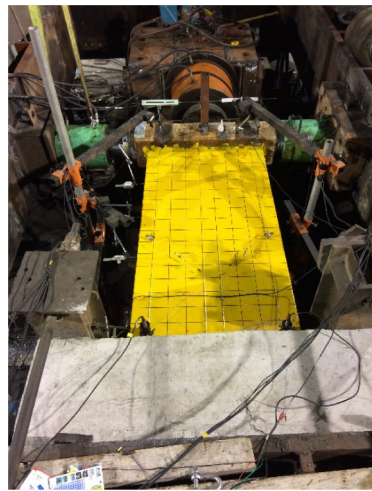
Table 1
Specimen parameters.

Specimen	$h \times b$ (mm \times mm)	H (mm)	t (mm)	Space of transverse stiffeners (mm)	Space of distributed batten plates (mm)	N_d (kN)	n_d	λ
CWS1	900 \times 100	1475	4	150	150	1983	0.50	1.64
CWS2	900 \times 100	1475	4	150	150	2975	0.75	1.64
CWS3	900 \times 100	1475	4	150	150	991	0.25	1.64
CWS4	900 \times 100	1025	4	150	150	1983	0.50	1.14
CWS5	900 \times 100	1925	4	150	150	1983	0.50	2.14
Original component	(2575–3300) \times (220–400)	4400	12	450	450	–	0.30–0.70	1.33–1.71

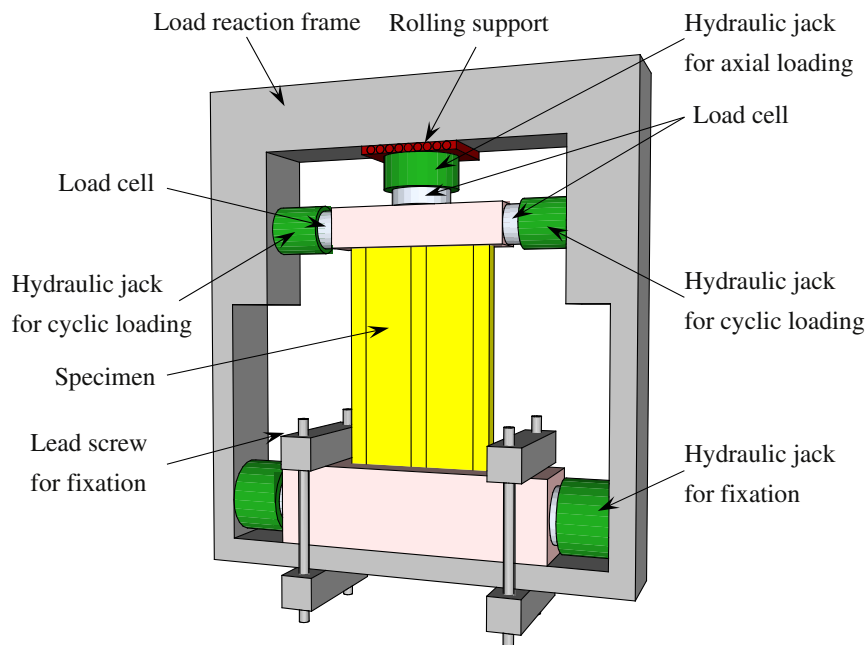
Notes: h and b are the cross-sectional width and thickness of the wall body, respectively; H is the height of composite wall; t is the thickness of the steel component; N_d is the axial applied load; n_d is the axial force ratio calculated by Eq. (1); λ is the shear span ratio calculated by Eq. (2).

The objective of the current paper is to investigate the seismic behaviour of this innovative CFDSC wall. Cyclic loading tests on five specimens are conducted to study the seismic behaviour of the wall considering the influence of the axial force ratio and shear span ratio.

The failure mode, hysteresis behaviour, strength and deformation capacity of the wall are discussed in details. Furthermore, formulae for evaluating the lateral load-carrying capacity of the wall are proposed and verified by the experimental results.



(a) Test setup for cyclic loading



(b) Loading and instrumentation

Fig. 4. Loading configuration.

2. Experimental program

2.1. Details of specimens

Five innovative CFDSC wall specimens, labelled as CWS1 to CWS5, were tested under cyclic lateral loading. The specimens were fabricated at approximately 1/3 scale because of size limitation of the testing equipment. The cross-sectional dimension of the specimens and the thickness of the steel component were reduced based on a typical CFDSC wall selected from the China Southern Airlines Building, while the steel ratio of the section and the width-to-thickness ratio of the steel plate remained consistent with the original one. The detailed dimensions of all the test specimens are shown in Fig. 3 and Table 1 (compared with that of the original full-scale CFDSC wall). Each specimen had identical cross-section dimension and reinforcement configurations except the height of the wall. The cross-sectional dimensions of the wall specimens were 900 mm in width and 100 mm in thickness, including three square CFST elements with the side length of 100 mm locating at the end and in the middle of the cross section. The thickness of the steel plate, the reinforcement and the steel tube in CFST columns was 4 mm. The spacing of the transverse stiffener and the vertical diaphragm was 150 mm, which was determined by limiting the width-to-thickness ratio of stiffened steel plate. The width-to-thickness ratio limitation value ($40\sqrt{235/f_y}$) according to the Chinese code for design of steel structures GB 50017 [17] was adopted. At the middle of each steel compartment that was divided by the transverse stiffener and the vertical diaphragm, a batten plate with the cross-sectional dimension of 4 mm × 10 mm was attached between the double steel plates. The wall was anchored in a strong RC foundation beam and a RC top beam for convenient installing and loading in the reaction frame. The variable parameters in the tests included the axial force ratio (n_d) and the shear span ratio (λ). The n_d and λ are calculated [11,14] by

$$n_d = \frac{1.2N_d}{f_c A_c / 1.4 + f_y A_s / 1.11} \quad (1)$$

$$\lambda = \frac{H}{h} \quad (2)$$

where N_d is the applied axial compressive force; f_c is the compressive strength of the wall concrete, which is taken as 0.76 times of the compressive strength from cubes of 150 mm in size [18]; f_y is the yield strengths of steel derived from the coupon test; A_c and A_s denote the gross cross-sectional areas of concrete and steel in the composite wall, respectively; H is the effective height of the wall, as marked in Fig. 3. It should be noted that the parameter 1.2 in Eq. (1) donates the load safety factor according to the Chinese code for design of concrete structures GB50010-2010 [18], and the parameter 1.4 and 1.11 represent the material strength reduction factors for the concrete and steel, respectively. The range of the values of the axial force ratio (n_d) and shear span ratio (λ) chosen for the test specimens were based on the practical design values of the typical CFDSC wall in the China Southern Airlines Building, as shown in Table 1.

2.2. Materials

The strength grade of the infill concrete for all the specimens was C40 whose characteristic value of cubic compressive strength is 40 MPa, according to GB 50010 [18]. Three cubes of 150 mm in size were manufactured to obtain the actual cubic compressive strength. The average value of the cubic compressive strength on the testing day was 42.2 MPa.

The steel grade of Q235 with nominal yield strength of 235 MPa [19] was selected for the steel components in the specimens. The actual yield

strength f_y , ultimate strength f_u , and elasticity modulus E_s attained from the coupon tests were 320.8 MPa, 462.4 MPa and 172.7 GPa, respectively.

2.3. Test set-up and loading procedure

The specimens were tested in the 20,000 kN load reaction frame, as shown in Fig. 4. The base of the specimen was clamped onto the reaction frame by the lead screws and the hydraulic. The axial compressive force was firstly applied to the designated values by using a 20,000 kN capacity hydraulic jack with rolling support. The axial compressive force kept constant during the whole lateral loading process. The axial compressive forces of each specimen are listed in Table 1. The cyclic loading was conducted by a couple of 2,000 kN capacity hydraulic jacks. The lateral force was applied by using displacement control method. The drift ratio of the specimen defined as the ratio of the lateral displacement to the effective height of the wall [11,20] was taken as the controlling parameter. As displayed in Fig. 5, the drift ratio was limited to be 1/300 at first loading step, which was increased subsequently to 1/150, 1/100, 1/75, 1/50 and 1/30. Three cycles were repeated at each drift ratio level. The test was terminated when the lateral resistance of the wall had dropped below 85% of its maximum strength or the axial force could not be sustained.

2.4. Measurements

The applied axial force and horizontal forces at the top of the CFDSC wall specimen were measured by the load cells which were located and fixed between the hydraulic jacks and the RC top beam, as Fig. 4(b) shows. Fig. 6 shows the locations of linear variable differential transducers (LVDTs) and strain gauges installed on the specimens. The transducers L1 and L2 were placed at the RC top beam corresponding to the lateral loading point to monitor the horizontal displacement of the specimen during the test. Three horizontal LVDTs (L3–L5) were installed along the height of the wall to measure the lateral displacement at different heights. L6 and L7 were mounted diagonally on the wall to measure the shear deformation. In addition, two vertical LVDTs (L8–L9) were installed on the foundation beam to monitor the possible displacement and rotation of the base. Strain gauges were arranged on the surface of the wall to measure the deformation of steel plate, as displayed in Fig. 6(b).

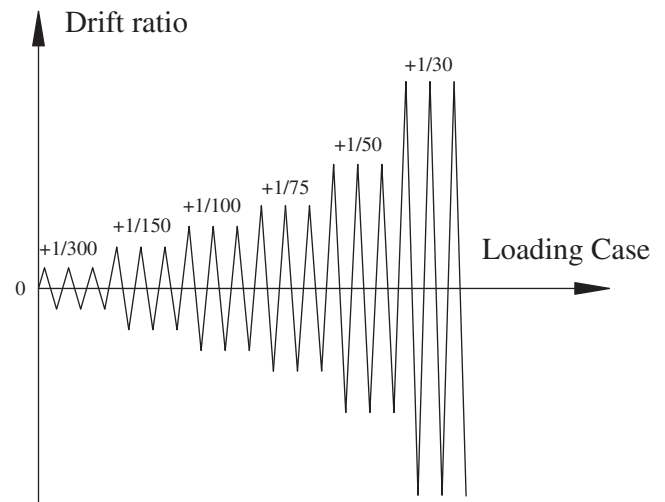
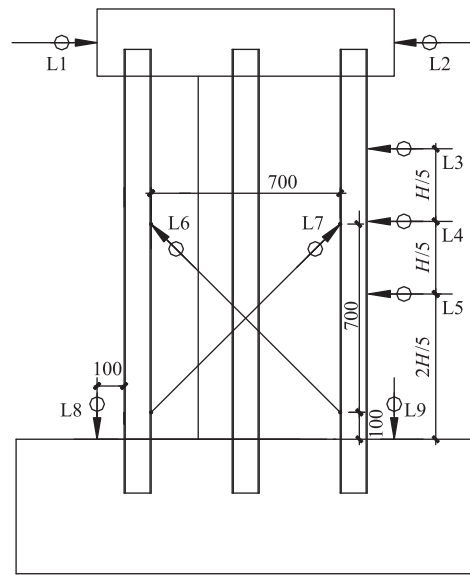
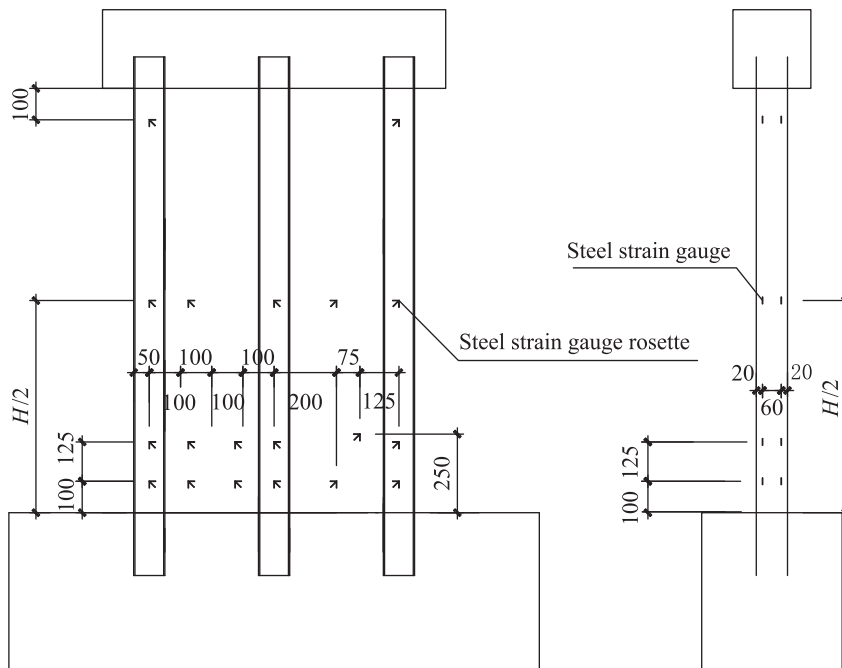


Fig. 5. Cyclic loading spectrum.



(a) Location of the displacement transducers



(b) Location of strain gauges

Fig. 6. Instrumentation arrangement.

3. Cyclic loading tests

3.1. Failure modes

All specimens experienced similar damage process including local buckling of steels before the peak load, and subsequent fracturing of the steel faceplates and the boundary CFST columns at the post-peak stage. According to the position of local buckling of the steels, two different failure modes, viz. failure mode I and failure mode II, were identified for the CFDS walls, as shown in Fig. 7(a) and (b) respectively. For all the specimens except CWS4 whose shear span ratio are equal or >1.64 , local buckling of the steels occurred in the region of $0.3H$ from the bottom of the wall, which were categorised as failure mode I. For

Specimen CWS4 whose shear span ratio is 1.14, the buckling position of the steels moved up to the mid-height of the wall, which was categorised as failure mode II.

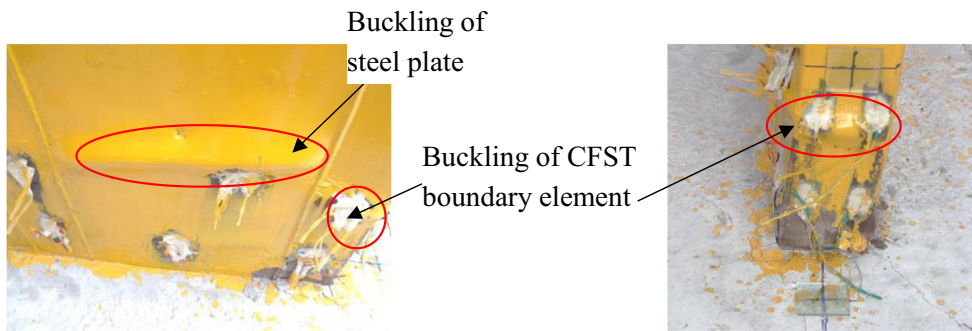
Taken Specimen CWS1 as an example to illustrate the experimental phenomenon in details for failure mode I, at the beginning of the test, the specimen behaved elastic response and no local buckling of the steel could be observed. As the drift ratio came to $1/150$ – $1/75$, the steel plates and the boundary CFST columns at the height of about 200 mm from the bottom reached its yield strain. During the drift ratio of $1/75$ – $1/50$, slight buckling was observed on the steel plates and the boundary CFST columns at the height of 250 mm from the base. The specimen reached its peak load at the drift ratio of $1/62$. After the peak load, the buckling of the steels became more serious



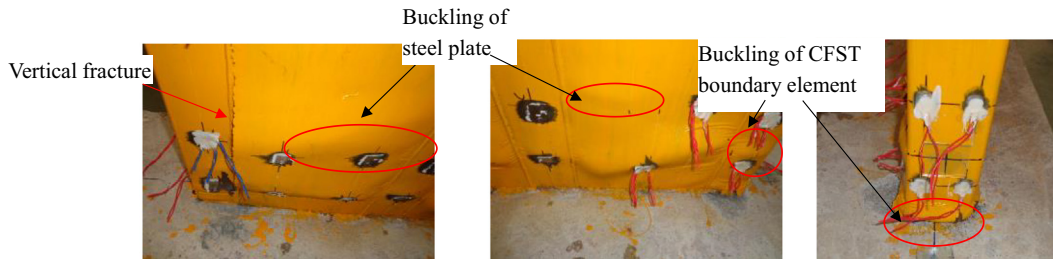
(a) Failure mode I for CWS1



(b) Failure mode II for CWS4



(c) Details of failure for CWS1



(d) Details of failure for CWS4

Fig. 7. Failure models from cyclic loading.

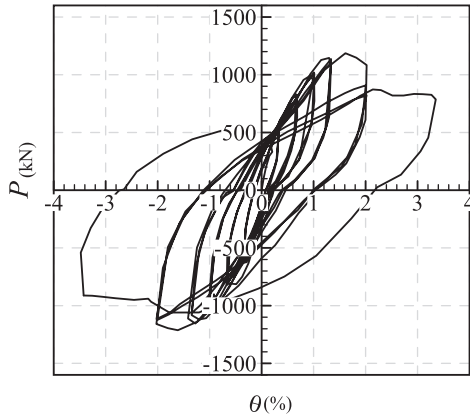
and gradually extended to the area of 350 mm from the bottom of the wall, which resulted in degradation of its lateral resistance. The test was terminated when the lateral force decreased to 85% of its peak load. The failure photograph of Specimen CWS1 is shown in Fig. 7(c). This failure mode occurred in specimens with relatively higher shear

span ratio ($\lambda \geq 1.64$), which was typical flexural failure mode of shear wall.

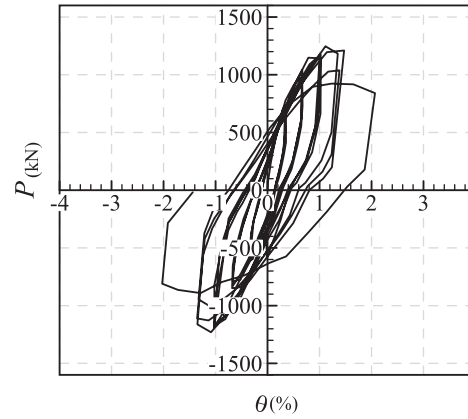
Specimen CWS4 is taken to illustrate the experimental phenomenon with failure mode II. No obvious deformation of the wall was observed when the drift ratio reached 1/150. During the drift ratio from 1/150

to 1/75, the boundary CFST elements and the steel plate at the height of 250 mm from the bottom began to reach its yield strain. When the drift ratio reached 1/75–1/50, slight buckling on the steels was discovered at the height of 450 mm from the bottom. In this period, the lateral force reached its maximum when the drift ratio was about 1/60. The buckling of the steels became more evident during the drift ratio of 1/50–1/30,

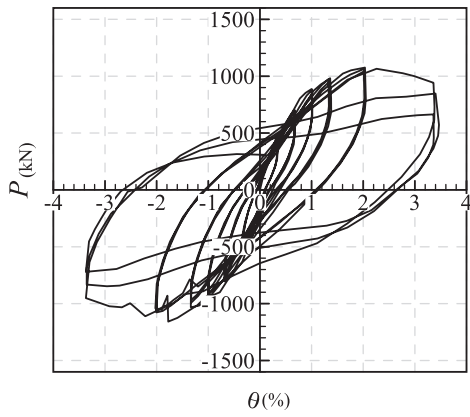
resulting in the deterioration of its lateral strength. The test was ended when the lateral force decreased to 85% of its peak load. The failure photograph of Specimen CWS4 is shown in Fig. 7(d). This failure mode appeared in the specimens with a relatively lower shear span ratio ($\lambda < 1.64$), which was typical flexure-shear failure mode of shear wall.



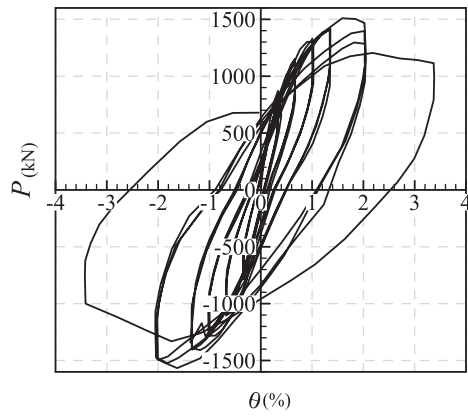
(a) CWS1



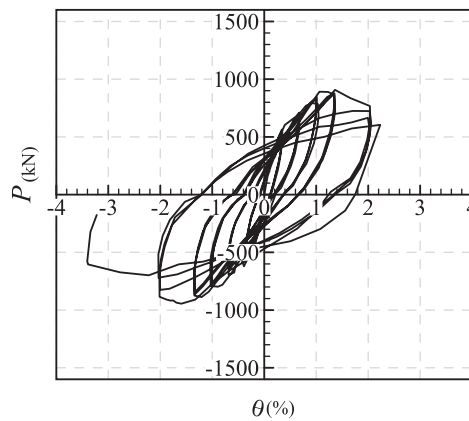
(b) CWS2



(c) CWS3



(d) CWS4



(e) CWS5

Fig. 8. Lateral load (P)–drift ratio (θ) hysteresis curves for specimens.

3.2. Hysteresis curves

Fig. 8 shows the lateral force (P) versus drift ratio (θ) hysteresis curves for all specimens under cyclic loading. The lateral load–drift ratio response was closely linear when the drift ratio was between 1/300–1/150. As the drift ratio increased to 1/150–1/75, the specimens entered the inelastic range. The hysteresis curves became spindle-shaped together with slight degradation of stiffness and strength. After that, the lateral resistance of the specimens reached the maximum strength. In the post-peak stage, the lateral resistance of the wall began to decline due to the severe buckling of the steels. Serious degradation of stiffness and strength could be observed in this stage, in which Specimen CWS2 ($n_d = 0.75$) exhibited the most unfavourable strength degradation. Little serious pinching effect was observed on the hysteresis curves of all the specimens at the ultimate drift ratio, which states great energy dissipation capacity of the CFDSC walls.

3.3. Skeletal curves and ductility

Fig. 9 gives the skeletal lateral force (P) versus drift ratio (θ) curves for all the specimens. The characteristic loads and their corresponding drift ratios including the positive (+) and negative (–) loading directions are listed in Table 2, in which P_y , P_m and P_u are the yield load, peak load and ultimate load for specimens, respectively; θ_y , θ_m and θ_u are the drift ratios corresponding to P_y , P_m and P_u , respectively. In order to quantify the ductility of the CFDSC wall in the post-peak stage, the ductility coefficients μ of the specimens are calculated by.

$$\mu = \theta_u / \theta_y \tag{3}$$

where θ_u is the drift ratio corresponding to a 15% strength degradation from the peak load [21]; θ_y is the drift ratio corresponding to the yield load which was determined by the general yield point method [22], where the yield load is defined as that corresponding to the intersection point of two tangent lines on the load–deformation curve, being the tangent line at one-third of the maximum strength and that at half of the deformation at maximum strength, as shown in Fig. 10(a). The calculation of the ductility ratio for each specimen is displayed in Fig. 10(b)–(f).

As shown in Fig. 9 and Table 2, the drift ratios corresponding to the ultimate stage were in the range from 1/67 to 1/30 with the ductility

Table 2
Measured characteristic strengths and drift ratios.

Specimen	Loading direction	P_y (kN)	θ_y	P_m (kN)	θ_m	P_u (kN)	θ_u	$\mu = \theta_u / \theta_y$
CWS1	+	625	1/266	1187	1/62	1009	1/48	5.54
	–	–627	1/290	–1213	1/62	–1031	1/48	6.04
CWS2	+	707	1/339	1247	1/90	1060	1/67	5.06
	–	–605	1/338	–1230	1/92	–1046	1/67	5.04
CWS3	+	652	1/169	1076	1/49	942	1/30	5.63
	–	–655	1/263	–1158	1/56	–984	1/32	8.22
CWS4	+	929	1/278	1509	1/63	1283	1/47	5.91
	–	–1025	1/207	–1566	1/61	–1331	1/46	4.50
CWS5	+	508	1/335	890	1/94	757	1/50	6.70
	–	–548	1/330	–944	1/63	–804	1/47	7.02

coefficients varying from 4.50 to 8.22, which indicated that all the specimens had excellent deformation capacity and exhibited ductile post-peak-load behaviour. As shown in Fig. 9(a), the increase of the axial compressive ratio could augment the initial stiffness and secant stiffness of the wall. This can be explained as follows: for CFDSC wall specimens failed by bending, as the increase of the axial force, higher initial compressive strain occurred at the bottom section of the CFDSC wall prior to lateral cyclic loading, which is benefit to restrain the premature tensile crack of concrete during the cyclic loading, leading to the augment of the lateral stiffness. In addition, the maximum lateral resistance of Specimen CWS1 ($n_d = 0.50$) and CWS2 ($n_d = 0.75$) were 4.7% and 7.7% higher than that of Specimen CWS3 ($n_d = 0.25$), respectively, which stated that the augment of axial compressive ratio was favourable for the strength of the specimens. However, the increasing axial compressive ratio would produce adverse effect on the ductility as the average ductility coefficients between the positive and negative loading directions of Specimens CWS3, CWS1 and CWS2 were 6.93, 5.79 and 5.05, respectively. Therefore, it is noted that proper axial compressive load is beneficial to the bearing capacity and lateral stiffness of the shear wall, which coincides with the observations presented in the previous studies [23–25].

As shown in Fig. 9(b), the influence of shear span ratio on the skeletal curves of CFDSC wall was substantial. As the shear span ratio increased, the initial stiffness and the maximum bearing capacities of the specimens declined dramatically. In details, the peak loads of

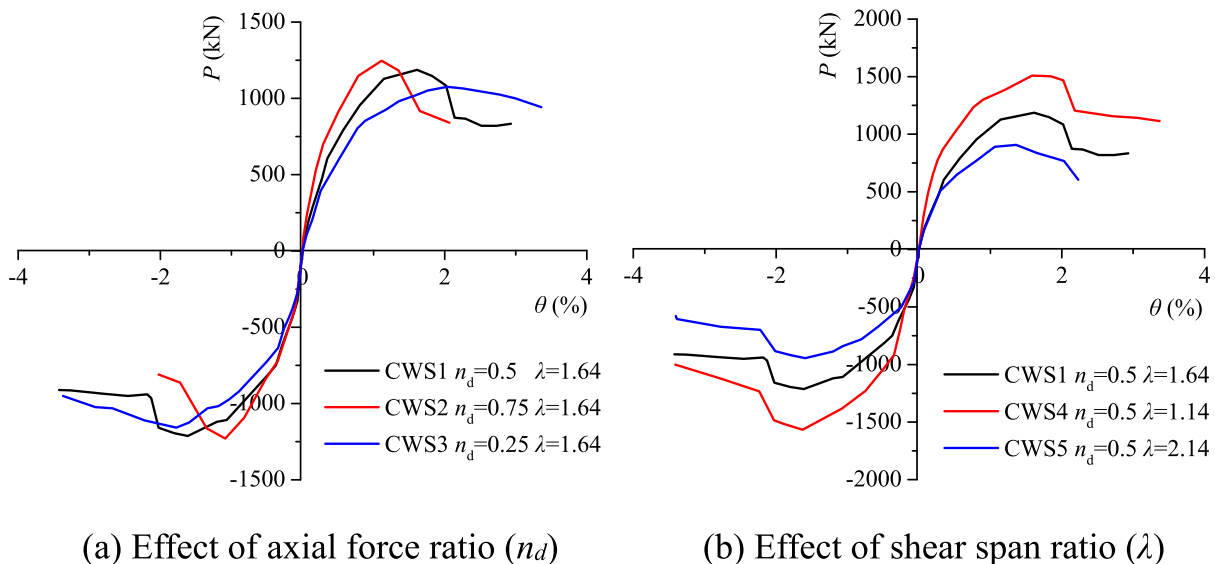
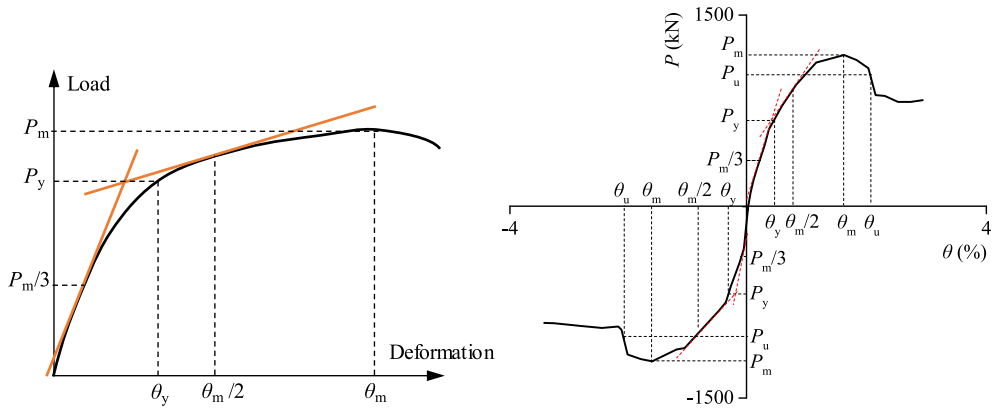
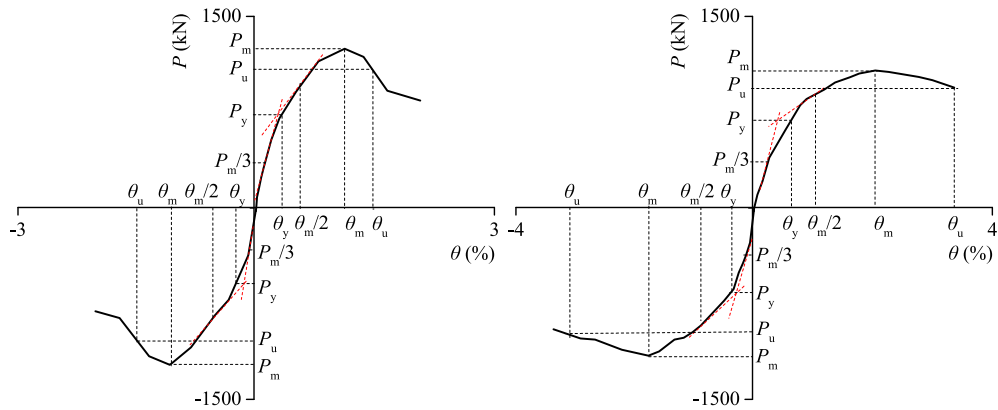


Fig. 9. Skeleton lateral force (P) versus drift ratio (θ) curves.



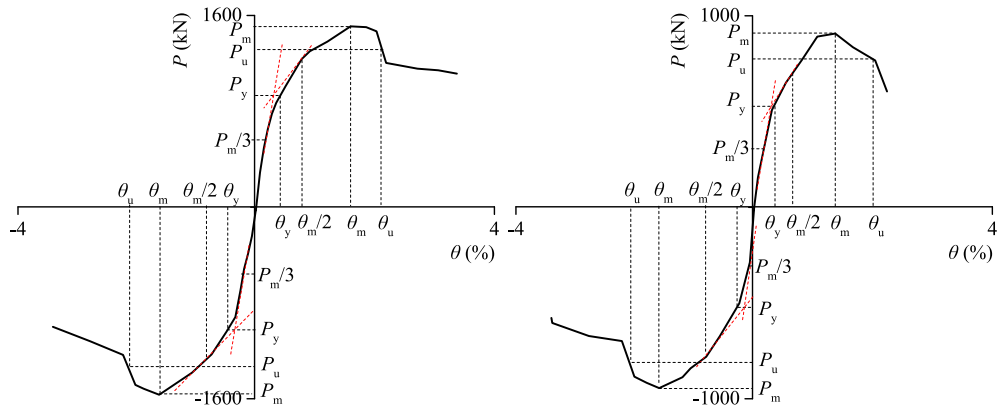
(a) Illustration of general yield point method.

(b)CWS1



(c)CWS2

(d)CWS3



(e)CWS4

(f)CWS5

Fig. 10. Calculation of ductility ratio for each specimen.

Specimens CWS1 ($\lambda = 1.64$) and CWS4 ($\lambda = 1.14$) were 28.4% and 65.9% higher than that of Specimen CWS5 ($\lambda = 2.14$), respectively. In addition, the larger shear span ratio was favourable to the ductility of the specimens as the average ductility coefficients between the positive and negative loading directions of Specimens CWS4, CWS1 and CWS5 are 5.21, 5.79 and 6.86, respectively.

3.4. Strength and stiffness degradation

To describe the strength degradation in the i th loading cycle at the j th load step, the strength degradation coefficient $\lambda_{i,j}$ is defined as [26].

$$\lambda_{i,j} = Q_{j, \max}^i / Q_{j, \max}^1 \quad (4)$$

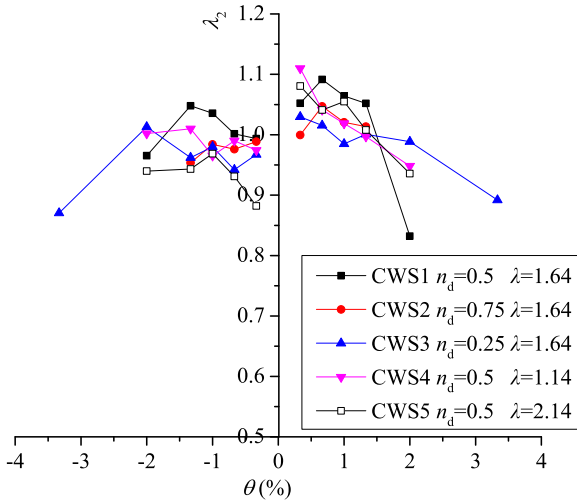


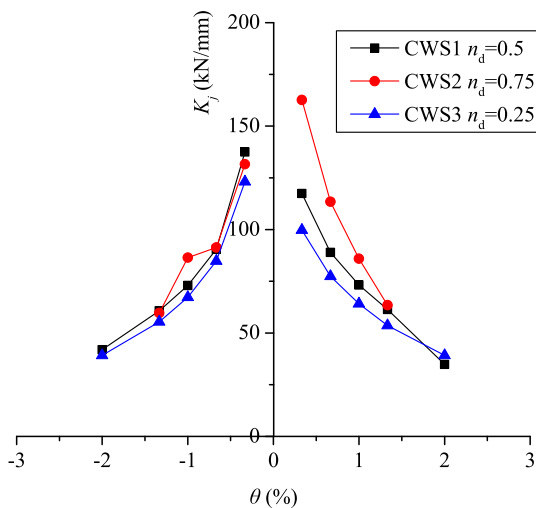
Fig. 11. Strength degradation curves for 2nd cycle of specimens.

where $Q_{j,max}^1$ and $Q_{j,max}^i$ are the peak load for the 1st and the i th loading cycle at the j th drift level respectively. Fig. 11 plots the strength degradation curves of the 2nd cycle for all the specimens. It can be seen that the values of $\lambda_{2,j}$ is in the range from 0.87 to 1.12, and some of them exceeds 1.0 before reaching the peak strength. After reaching the peak strength, $\lambda_{2,j}$ decreases evidently due to the severe buckling and fracture of the steels.

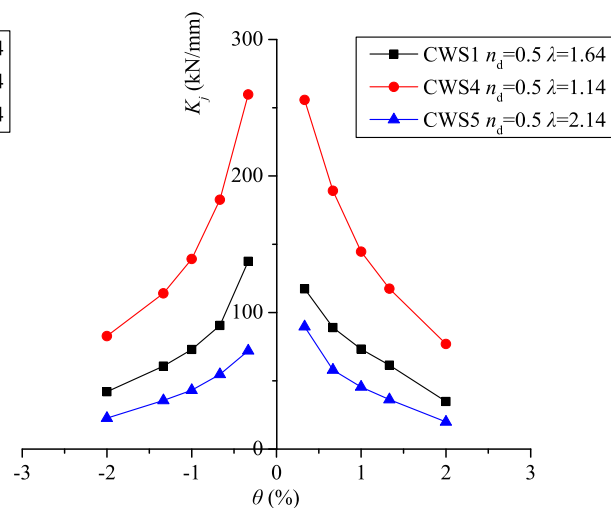
The secant stiffness of the envelope curves at each load step is adopted to describe the stiffness degradation (K_j) [27], which is expressed as:

$$K_j = \frac{\sum_{i=1}^m | +P_{i,j} | + | -P_{i,j} |}{\sum_{i=1}^m | +X_{i,j} | + | -X_{i,j} |} \quad (5)$$

where $+P_{ij}$ ($-P_{ij}$) is the positive (negative) peak load in the i th loading cycle at the j th drift ratio step, and $+X_{ij}$ ($-X_{ij}$) is the displacement corresponding to the positive (negative) peak load in the i th loading cycle at the j th drift ratio step; and m denotes the number of loading cycles.



(a) Effect of axial force ratio (n_d)



(b) Effect of shear span ratio (λ)

Fig. 12. Secant stiffness curves for specimens.

The relationships of the secant stiffness versus the drift angle for all the specimens are plotted in Fig. 12. It can be observed that the secant stiffness of the specimen degraded with the drift angle increasing. As shown in Fig. 12(a), the increase of axial force ratio could intensify the secant stiffness but lead to severer stiffness degradation in the positive loading direction, although the influence was limited in the negative loading direction. As shown in Fig. 12(b), the effect of shear span ratio on the stiffness degradation was significant. The decline of the shear span ratio would evidently enlarge the secant stiffness of the specimen. However, the decrease of shear span ratio was disadvantageous to the stiffness degradation of the specimen since the slope of the degradation curve was steeper for the ones with smaller shear span ratio.

3.5. Energy dissipation capacity

The energy dissipated in each loading cycle is equal to the area enclosed by the corresponding hysteresis loop, which could be calculated from the lateral load versus lateral displacement curve. The relationships between energy dissipation (E) and drift ratio (θ) for each cyclic step are depicted in Fig. 13. The CFSDC wall specimens tended to induce larger amount of dissipated energy as the drift ratio increased. Also, the discrepancy of energy dissipation between different specimens enlarged in post-yielding stage. By comparing the effect of axial force ratio and shear span ratio on the energy dissipation of the specimens at a specific drift ratio, it is found out that the larger axial force ratio or shear span ratio was favourable to the dissipated energy of the CFSDC wall specimens. However, premature failure of the specimens with higher axial force ratio (CWS2) resulted in the loss of energy dissipation capacity at the last drift ratio of 1/30.

3.6. Strain

The measured vertical strains of the boundary CFST column (ϵ) versus drift ratio of specimens (θ) in CWS2 are shown in Fig. 14, where the tensile and compressive strains are considered as positive and negative, respectively. It shows that the absolute values between compressive strains and tensile strains at each drift ratio were almost equal before the specimen fractured. The strains of boundary CFST element reached its yield strain at the drift ratio of 1% (which was close to drift ratio corresponding to the peak load). Compared the maximum attainable strains along the height of the boundary CFST column during the test,

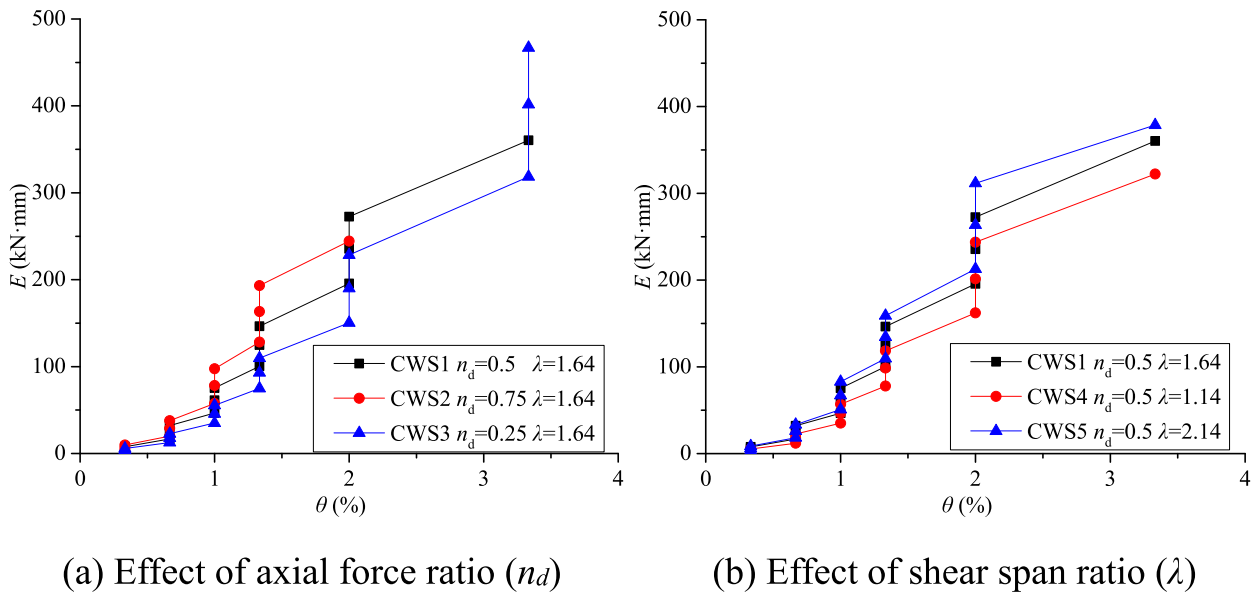


Fig. 13. Cumulative energy dissipation.

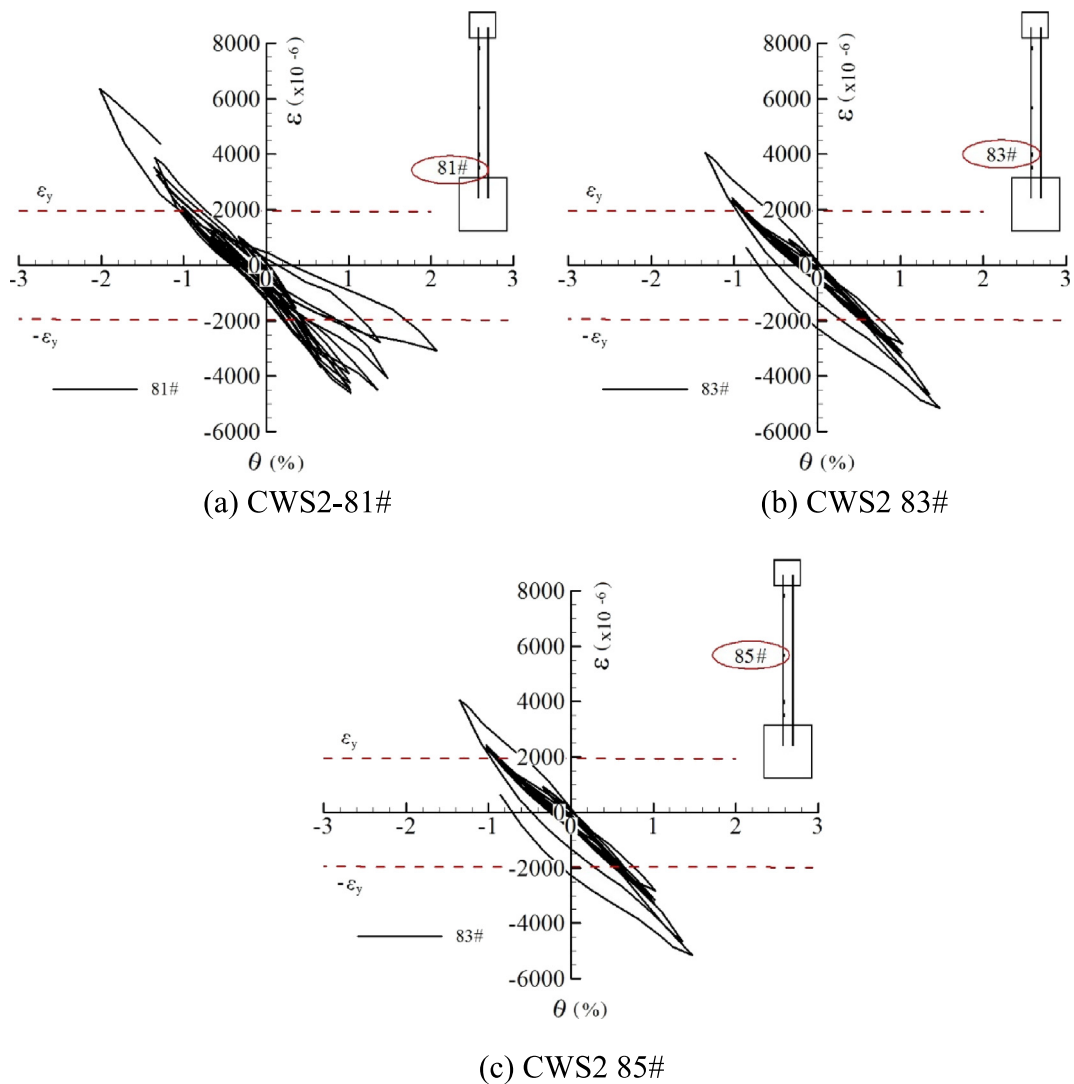


Fig. 14. Vertical strains (ϵ) versus drift ratio (θ) curves for Specimen CWS2.

the one located at the bottom was larger than those in the upper position.

The distributions of the longitudinal strains along the width of the wall for Specimens CWS3 and CWS4 are shown in Fig. 15, which are extracted from the negative loading direction in the first cycle at each drift ratio step. For Specimen CWS3, the longitudinal strains were approximately linearly distributed along the width of the wall throughout the loading process (Fig. 15(a)). Similar features could be recognized for all the other specimens with failure mode I, which illustrates that the plane section assumption can be adopted for these specimens. However, for Specimen CWS4 with failure mode II, the longitudinal strains of compressive boundary CFST elements were much greater than the others, which conflicts with the plane section assumption.

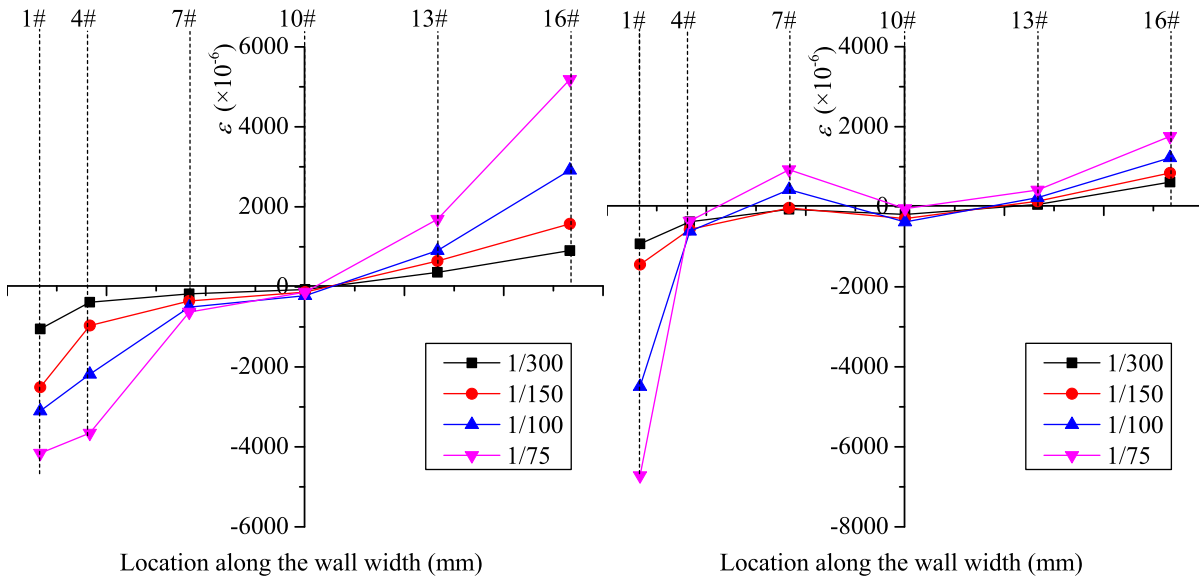
4. Load-carrying capacity

The plastic stress distribution method (PSDM) [28,29] is an equilibrium-based method to resolve the resistance of a composite cross-section under combined compression and bending, which is also included in Eurocode [30] and AISC [31]. In PSDM, perfect bond exists

between the concrete and steel plate, and plane sections are assumed to remain plane under bending with full plastic stresses of materials distribution over the composite cross section. Previously, simplified design methods based on PSDM for calculating the strength of the composite wall have been proposed by Eom et al. [2], Ji et al. [9] and Hu et al. [32]. However, none of these simplified design methods considers the confinement effect from steel plates which can increase the effective compressive strength of the core concrete in the CFDSC wall. Especially, the cross section of the CFDSC wall proposed in this paper was divided into compartments by continuous longitudinal steel diaphragm, which is similar to the combination of several rectangular CFST columns. Thus, the confinement effect from the steel plates on the inner concrete should not be ignored. In this paper, a calculation method considering the confined concrete strength is proposed to predict the lateral load-carrying capacities of the CFDSC wall.

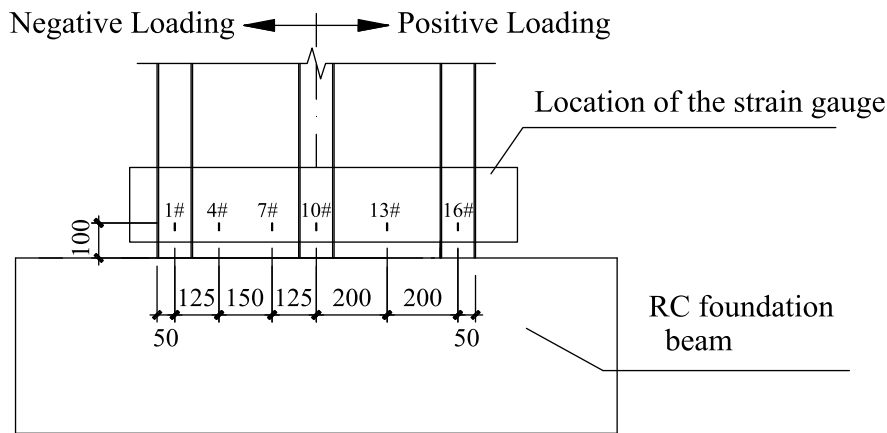
4.1. Calculation method

According to PSDM, plastic stress distributions and the equilibrium condition of the cross section are shown in the Fig. 16. Based on the



(a) CWS3

(b) CWS4



(c) Location of strain gauges along the wall

Fig. 15. Distribution of the longitudinal strains along the wall width of specimens CWS3 and CWS4.

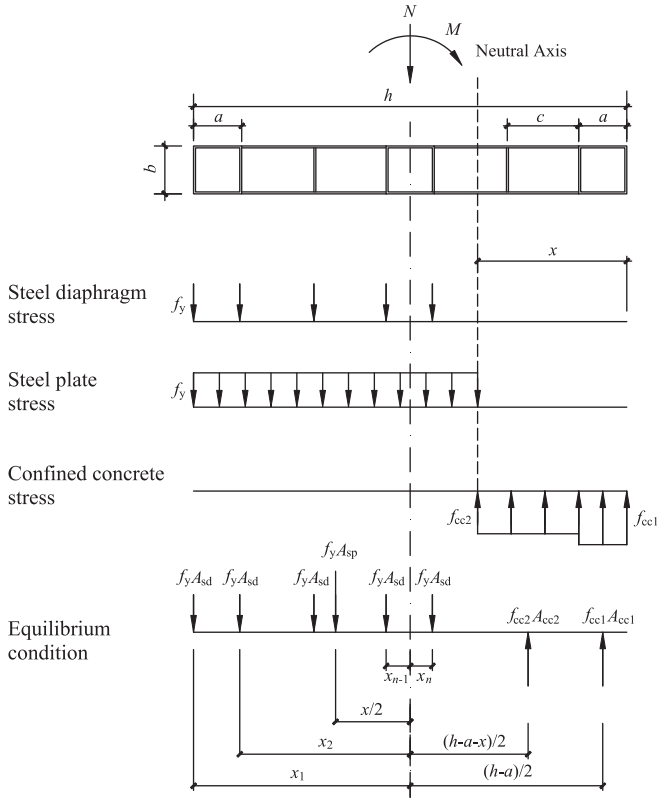


Fig. 16. Plastic stress distributions of innovative shear walls.

equilibrium condition in Fig. 16, the axial compressive force N can be determined from an assumed neutral axis depth x , which is expressed as:

$$N = f_{cc1}A_{cc1} + f_{cc2}A_{cc2} - f_y A_{sp} - n f_y A_{sd} \quad (6)$$

$$= f_{cc1}ab + f_{cc2}(x-a)b - 2f_y(h-x)t - n f_y(b-2t)t$$

where N is the axial load applied on the wall; f_{cc1} and f_{cc2} are the effective compressive strength of the boundary CFST elements and CFDSC wall body, respectively; A_{cc1} and A_{cc2} are the compressive area of the boundary CFST elements and CFDSC wall body, respectively; f_y is yield strength of the steel and is taken as 320.8 MPa from the standard coupon test; A_{sp} and A_{sd} are the area of the tensile steel faceplate and steel diaphragm, respectively; n is the number of steel diaphragm in tension; h and b are the width and the thickness of the CFDSC wall, respectively; a is the side length of the boundary CFST column; c is the space between the adjacent longitudinal steel diaphragms; t is the thickness of the steel.

As mentioned above, the cross section of the CFDSC wall is like the combination of several rectangular CFST columns. Thus, the effective compressive strengths of the boundary CFST elements and CFDSC wall body are determined by Eqs. (7)–(10) for calculating the effective compressive strength of rectangular CFST columns according to DBJ 13-51-2010 [33], which takes account of the confinement effect for the CFST columns by the confining factor ξ .

$$f_{cc1} = f_c(1.18 + 0.85\xi_1) \quad (7)$$

$$\xi_1 = \frac{f_y A_{s1}}{f_c A_{c1}} = \frac{f_y [ab - (a-2t)(b-2t)]}{f_c (a-2t)(b-2t)} \quad (8)$$

$$f_{cc2} = f_c(1.18 + 0.85\xi_2) \quad (9)$$

Table 3
Comparison of the calculated and test load-carrying capacities for each specimen.

Specimen	Loading direction	P_m (kN)	P_{cal} (kN)	P_{cal}/P_m	P_e (kN)	P_e/P_m
CWS1	+	1187	1058	0.89	596	0.50
	–	1213	1058	0.87	596	0.49
CWS2	+	1247	976	0.78	482	0.39
	–	1230	976	0.79	482	0.39
CWS3	+	1076	1042	0.97	621	0.58
	–	1158	1042	0.90	621	0.54
CWS4	+	1509	1523	1.01	858	0.57
	–	1566	1523	0.97	858	0.55
CWS5	+	890	811	0.91	434	0.49
	–	944	811	0.86	434	0.46
				Mean value	0.90	0.49
				COV	0.07	0.07

$$\xi_2 = \frac{f_y A_{s2}}{f_c A_{c2}} = \frac{f_y [bc - (b-2t)(c-2t)]}{f_c (b-2t)(c-2t)} \quad (10)$$

By Eq. (6), the depth of the compression zone (x) can be calculated as:

$$x = \frac{N - (f_{cc1} - f_{cc2})ab + 2f_y ht + n f_y (b-2t)t}{f_{cc2}b + 2f_y t} \quad (11)$$

After determining the depth of the compression zone (x), the flexural strength (M) can be calculated from:

$$M = \frac{1}{2} f_{cc1} A_{cc1} (h-a) + \frac{1}{2} f_{cc2} A_{cc2} (h-a-x) + \frac{1}{2} f_y A_{sp} x + \sum_{i=1}^n x_i \cdot f_y A_{sd} \quad (12)$$

where x_i is the distance from each tensile steel diaphragm to the central axis. The lateral load-carrying capacity (P_{cal}) of the CFDSC wall is calculated by:

$$P_{cal} = M/H \quad (13)$$

4.2. Verification

Table 3 lists the maximum experimental force P_m for all CFDSC specimens comparing with the theoretical results P_{cal} predicted by the proposed design model. It can be found that both results have satisfactory agreement. The mean value of P_{cal}/P_m is 0.90 with the coefficient of variation (COV) of 0.07. For comparison, the predictions P_e calculated by the formulae proposed by Hu et al. [32] are also included in Table 3. It can be seen from this table that the values of P_e excessively underestimate the actual lateral resistance of the CFDSC walls, which was attributed to the ignorance of the confinement effect from steel plate on the concrete strength. It can be concluded that the proposed design method is suitable to be used for predicting the strength of the CFDSC wall subjected to combined compression and bending. It is also worth noting that although the predicted results of Specimen CSW4 are in good agreement with the experimental ones, the accuracy of the proposed design method for predicting the strength of the CFDSC wall failed by flexure-shear mode still need to be further validated in future study due to the limited number of specimen in this test.

5. Conclusions

This paper presented an innovative composite shear wall consisting of the concrete filled double steel plate wall body and CFST boundary columns, in which the double steel plates are divided into compartments by continuous longitudinal steel diaphragm, and the transverse stiffeners and distributed batten plates were welded on the steel plate

of the wall body to strengthen the composite wall. The seismic behaviour of the composite shear wall was evaluated by cyclic tests. The following conclusions can be drawn based on the results from this study:

- (1) All specimens experienced similar damage process including local buckling of steels before the peak load, and subsequent fracturing of the steel faceplates and the boundary CFST columns at the post-peak stage. For the specimens whose shear span ratio are equal or >1.64 , local buckling of the steels occurred in the region of $0.3H$ from the bottom of the wall and the wall specimens were failed by flexural mode. For the specimen whose shear span ratio is 1.14, the buckling position of the steels moved up to position that is close to the mid-height of wall and the specimen was failed by flexure-shear mode.
- (2) Little serious pinching effect was observed on the hysteresis curves of all the specimens in which the drift ratios corresponding to the ultimate stage were in the range from $1/67$ to $1/30$ and the ductility coefficients were varied from 4.50 to 8.22, which states great seismic capacity of the CFDS walls.
- (3) The increase of the axial force ratio in the range from 0.25 to 0.75 could increase the initial stiffness and the secant stiffness of the skeletal curve as well as the peak strength of the specimen, but could produce adverse effects on the ductility, stiffness degradation and total energy dissipation of the CFDS walls. The decrease of shear span ratio could enhance the initial stiffness, the secant stiffness and the peak strength of the specimen. Whereas, the specimens with smaller shear span ratio had worse secant stiffness degradation, ductility and energy dissipation capacity.
- (4) The longitudinal strains were approximately linearly distributed along the width of the wall throughout the loading process for the specimens whose shear span ratio was equal or >1.64 .
- (5) Formulae for calculating the lateral load-carrying capacity of this type of composite shear wall, considering the confinement effect from steel plates on the core concrete strength, were proposed. The predictions of the lateral strength of CFDS wall agreed well with experimental results.

It should be noted that the CFDS walls in this paper performed flexural failure and flexure-shear failure modes. Besides, the shear failure mode may occur in the squat CFDS walls. Thus, the experiment for CFDS walls with shear failure mode and flexural-shear failure mode will be further conducted and reported in a future article.

Acknowledgements

This study was funded by the National Natural Science Foundation of China (51578246), Science and Technology Program of Guangzhou, China (201704020149), Natural Science Foundation of Guangdong Province, China (2016A030310418, 2017A030313263), Pearl River S&T Nova Program of Guangzhou, China (201806010137), State Key Lab of Subtropical Building Science, South China University of Technology (2018ZC11).

References

- [1] K.M.A. Hossain, S. Raffei, M. Lachemi, K. Behdinin, Structural performance of profiled composite wall under in-plane cyclic loading, *Eng. Struct.* 110 (2016) 88–104.
- [2] T.-S. Eom, H.-G. Park, C.-H. Lee, J.-H. Kim, I.-H. Chang, Behavior of double skin composite wall subjected to in-plane cyclic loading, *J. Struct. Eng.* 135 (2009) 1239–1249.
- [3] Y. Luo, X. Guo, J. Li, Z. Xiong, L. Meng, N. Dong, et al., Experimental research on seismic behaviour of the concrete-filled double-steel-plate composite wall, *Adv. Struct. Eng.* 18 (2016) 1845–1858.
- [4] M. Kwok, C. Gibbons, J. Tsui, P. Liu, Y. Wang, G. Ho, The structural design of the mega tower, China world trade Centre phase 3, Beijing China, *Prog. Steel Build. Struct.* 9 (2005) 1–6.
- [5] H.D. Wright, S.C. Gallocher, The behaviour of composite walling under construction and service loading, *J. Constr. Steel Res.* 35 (1995) 257–273.
- [6] K.M.A. Hossain, H.D. Wright, Performance of profiled concrete shear panels, *J. Struct. Eng.* 124 (1998) 368–381.
- [7] K.M. Anwar Hossain, H.D. Wright, Experimental and theoretical behaviour of composite walling under in-plane shear, *J. Constr. Steel Res.* 60 (2004) 59–83.
- [8] M.A.H. Khandaker, D.W. Howard, Design aspects of double skin profiled composite framed shearwalls in construction and service stages, *Struct. J.* 101 (2004) 94–102.
- [9] X. Ji, F. Jiang, J. Qian, Seismic behavior of steel tube-double steel plate-concrete composite walls: experimental tests, *J. Constr. Steel Res.* 86 (2013) 17–30.
- [10] L. Chen, H. Mahmoud, S.-M. Tong, Y. Zhou, Seismic behavior of double steel plate-HSC composite walls, *Eng. Struct.* 102 (2015) 1–12.
- [11] J.-G. Nie, H.-S. Hu, J.-S. Fan, M.-X. Tao, S.-Y. Li, F.-J. Liu, Experimental study on seismic behavior of high-strength concrete filled double-steel-plate composite walls, *J. Constr. Steel Res.* 88 (2013) 206–219.
- [12] J.-G. Nie, X.-W. Ma, M.-X. Tao, J.-S. Fan, F.-M. Bu, Effective stiffness of composite shear wall with double plates and filled concrete, *J. Constr. Steel Res.* 99 (2014) 140–148.
- [13] H.-S. Hu, J.-G. Nie, M.R. Eatherton, Deformation capacity of concrete-filled steel plate composite shear walls, *J. Constr. Steel Res.* 103 (2014) 148–158.
- [14] X. Zhang, Y. Qin, Z. Chen, L. Jie, Experimental behavior of innovative T-shaped composite shear walls under in-plane cyclic loading, *J. Constr. Steel Res.* 120 (2016) 143–159.
- [15] K. Ma, B. Liu, H. Yan, Q. Zhang, Experimental investigation on aseismic behavior of dual steel high strength concrete shear walls with high axial load ratio, *Eng. Mech.* 31 (2014) 218–224.
- [16] X. Fang, Q. Li, H. Wei, Y. Zhou, Y. Jiang, H. Lai, Experimental study on axial-flexural behavior of shear walls with steel tube-confined high performance concrete, *J. Build. Struct.* 34 (2013) 72–81.
- [17] J. Qian, Z. Jiang, X. Ji, Behavior of steel tube-reinforced concrete composite walls subjected to high axial force and cyclic loading, *Eng. Struct.* 36 (2012) 173–184.
- [18] GB 50010-2010, Code for Design of Concrete Structures, China Architecture & Building Press, Beijing, 2010.
- [19] G.B. 50017-2003, Code for Design of Steel Structures, China Planning Press, Beijing, 2010.
- [20] Y.-T. Wang, J. Cai, Y.-L. Long, Hysteretic behavior of square CFT columns with binding bars, *J. Constr. Steel Res.* 131 (2017) 162–175.
- [21] Q.-J. Chen, J. Cai, M.A. Bradford, X. Liu, Z.-L. Zuo, Seismic behaviour of a through-beam connection between concrete-filled steel tubular columns and reinforced concrete beams, *Eng. Struct.* 80 (2014) 24–39.
- [22] Y. Harada, K. Morita, Design of wide-flange section column-to-split-tee tensile connection with high-strength bolts, *J. Struct. Eng.* 133 (2007) 335–346.
- [23] F.-Y. Liao, L.-H. Han, Z. Tao, Performance of reinforced concrete shear walls with steel reinforced concrete boundary columns, *Eng. Struct.* 44 (2012) 186–209.
- [24] Wu Y-t, Kang D-y, Y.-B. Yang, Seismic performance of steel and concrete composite shear walls with embedded steel truss for use in high-rise buildings, *Eng. Struct.* 125 (2016) 39–53.
- [25] W. Wang, Y. Wang, Z. Lu, Experimental study on seismic behavior of steel plate reinforced concrete composite shear wall, *Eng. Struct.* 160 (2018) 281–292.
- [26] A. He, J. Cai, Q.-J. Chen, X. Liu, P. Huang, X.-L. Tang, Seismic behaviour of steel-jacket retrofitted reinforced concrete columns with recycled aggregate concrete, *Constr. Build. Mater.* 158 (2018) 624–639.
- [27] F.-Y. Liao, L.-H. Han, Z. Tao, Seismic behaviour of circular CFST columns and RC shear wall mixed structures: experiments, *J. Constr. Steel Res.* 65 (2009) 1582–1596.
- [28] H.D. Wright, T.O.S. Oduyemi, H.R. Evans, The design of double skin composite elements, *J. Constr. Steel Res.* 19 (1991) 111–132.
- [29] M. Xie, J.C. Chapman, Developments in sandwich construction, *J. Constr. Steel Res.* 62 (2006) 1123–1133.
- [30] EN 1994-1-1:2004, Eurocode 4: Design of Composite Steel and Concrete Structures – Part 1–1: General Rules and Rules for Buildings, European Committee for Standardization (CEN), Brussels, 2004.
- [31] American Institute of Steel Construction (AISC), Specification for Structural Steel Buildings. AISC 360-16, Chicago (IL), 2016.
- [32] H.-S. Hu, J.-G. Nie, J.-S. Fan, M.-X. Tao, Y.-H. Wang, S.-Y. Li, Seismic behavior of CFST-enhanced steel plate-reinforced concrete shear walls, *J. Constr. Steel Res.* 119 (2016) 176–189.
- [33] DBJ 13-51-2010, Development of Fujian Province, Technical Specification for Concrete-filled Steel Tubular Structures, Department of Housing and Urban, 2010.